10-2009

Analysis of the Wicking and Thin-Film Evaporation Characteristics of Microstructures

Ram Ranjan
Purdue University - Main Campus, ranjanr@purdue.edu

Jayathi Y. Murthy
School of Mechanical Engineering, Purdue University, jmurthy@purdue.edu

Suresh Garimella
School of Mechanical Engineering, sureshg@purdue.edu

Analysis of the Wicking and Thin-Film Evaporation Characteristics of Microstructures

Ram Ranjan

Jayathi Y. Murthy

Suresh V. Garimella[1]
e-mail: sureshg@purdue.edu

School of Mechanical Engineering and
Birck Nanotechnology Center,
Purdue University,
West Lafayette, IN 47907-2088

The topology and geometry of microstructures play a crucial role in determining their heat transfer performance in passive cooling devices such as heat pipes. It is therefore important to characterize microstructures based on their wicking performance, the thermal conduction resistance of the liquid filling the microstructure, and the thin-film characteristics of the liquid meniscus. In the present study, the free-surface shapes of the static liquid meniscus in common microstructures are modeled using SURFACE EVOLVER for zero Bond number. Four well-defined topologies, viz., surfaces with parallel rectangular ribs, horizontal parallel cylinders, vertically aligned cylinders, and spheres (the latter two in both square and hexagonal packing arrangements), are considered. Nondimensional capillary pressure, average distance of the liquid free-surface from solid walls (a measure of the conduction resistance of the liquid), total exposed area, and thin-film area are computed. These performance parameters are presented as functions of the nondimensional geometrical parameters characterizing the microstructures, the volume of the liquid filling the structure, and the contact angle between the liquid and solid. Based on these performance parameters, hexagonally-packed spheres on a surface are identified to be the most efficient microstructure geometry for wicking and thin-film evaporation. The solid-liquid contact angle and the nondimensional liquid volume that yield the best performance are also identified. The optimum liquid level in the wick pore that yields the highest capillary pressure and heat transfer is obtained by analyzing the variation in capillary pressure and heat transfer with liquid level and using an effective thermal resistance model for the wick. [DOI: 10.1115/1.3160538]

1 Introduction

Heat pipes have proven to be one of the most efficient passive cooling devices for electronics cooling and other applications. Heat pipes use porous media for wicking fluid from the condenser to the evaporator section. Wicking is caused by capillary forces acting at the solid-liquid-vapor contact line in the fluid-filled interstices in a porous medium. Wicking action, combined with evaporation in the evaporator section, causes fluid to move from the condenser to the evaporator; the amount of fluid flow that results depends on the permeability of the wicking medium. Furthermore, the effective thermal conductivity of the porous medium determines the effectiveness with which the heat is transferred to the evaporating fluid. With the increasing power density of critical electronic components, there is a need to optimize heat pipe microstructures to maximize the heat transfer rate and to minimize thermal resistance.

Avoiding dryout and overheating in heat pipes is a critical consideration and has been the focus of much research over the past few years. Many studies have proposed methods to develop permeability measurement techniques, to characterize wick porosity, and to quantify the overall performance of heat pipes. Most have focused on determining dryout heat fluxes and the limits of operation for a given wicking mechanism. Iverson et al. [1] quantified wick performance, including evaporation rates, for sintered-copper powder wicks under conditions of operation in heat pipes. They compared the performance of four different sintered wicks of varying porosity. The evaporative thermal resistance across thin layers of sintered-copper wicks of varying porosity was experimentally measured under saturated conditions by Davis and Garimella [2]. Numerical models for the effective thermal conduc-

tivity for various types of wicks have also been developed [3,4]. Garimella and Sobhan [5] reviewed the state of the art in the understanding and analysis of a large variety of heat pipes, and also identified the respective limitations. Maximum heat transfer rates for wrapped wire screen, square axial grooves, and sintered metal powder wicks were reported by Gupta and Upadhya [6]. They found sintered metal powder wicks to be the most effective for heat transfer. Abhat and Seban [7] performed experiments to study boiling and evaporation from heat pipe wicks with water and acetone. They postulated that the evaporative performance of a wick can be limited as much by a failure of capillary suction as due to fluid friction in the wick.

Thin-film evaporation, which takes place near a solid-liquid-vapor junction, is believed to be the dominant mode of heat transfer in such systems. Thin-film evaporation has been reported to affect the overall heat transfer capability in sintered porous media [8]. A theoretical model for thin-film evaporation was developed by Wang et al. [9,10]. The model predicts that more than 50% of the total heat transfer from the evaporating meniscus occurs in the microregion of the meniscus.

Numerical and theoretical models have also been developed for the operation of heat pipes [11] and to delineate the role of thin-film evaporation in such systems [8]. Kim et al. [12] proposed a one-dimensional mathematical model for a miniature heat pipe with a grooved wick structure to predict its thermal performance characteristics. Do et al. [13] presented a mathematical model to analyze the thermal characteristics of a flat microheat pipe with a grooved wick. Axial variations in wall temperature and the evaporation and condensation rates were also included in the model. Mwaba et al. [14] studied the influence of wick characteristics on heat pipe performance using numerical methods. They considered screen-mesh and sintered-copper wicks as the porous medium in heat pipes and pointed out that a heat pipe with a composite wick structure gives the best performance. Hanlon and Ma [8] presented a two-dimensional model to predict the overall heat trans-

fer capability of a sintered wick structure. They concluded that thin-film evaporation from the top surface of the sintered wick plays a major role in enhancing heat transfer. Failure to establish an adequate thin-film evaporation condition on the top surface of the wicks was shown to result in a significant decrease in the rate of evaporation.

Evaporation from liquid menisci in complex geometries has also been studied [15,16]. Morris [17] developed a theoretical model to predict apparent contact angles for evaporating liquids. Another study by Morris [18] provided a relationship between heat flow, apparent contact angle, interface curvature, superheat, and material properties for a perfectly wetting system; a conduction model with a fixed liquid-vapor interface was considered for estimating heat flow across the interface for small capillary number flows with thermocapillary and bulk flow effects being ignored. Transport from a volatile meniscus inside an open microtube was modeled by Wang et al. [19]. This work delineated the structure of fluid flow near an evaporating meniscus, including Marangoni and buoyancy-driven instabilities. Recently, Dhavaleswarapu et al. [20] visualized flow patterns near an evaporating meniscus using μPIV techniques and compared the influence of buoyancy and thermocapillarity on the overall flow structure. These studies have led to a better understanding of an evaporating liquid meniscus and are useful in providing guidelines for the design of efficient microstructures for passive cooling devices.

We seek to develop the basis for reverse-engineering the porous-medium microstructure to yield the optimum combination of capillary pressure, permeability, and thermal conductivity. In this paper, we address the issue of which microstructure geometries yield the maximum wicking action, as well as optimal thin-film heat transfer characteristics. We use SURFACE EVOLVER [21] for computing the static liquid meniscus shapes in different microstructures. This program has been used in the literature [22,23] to compute liquid capillary surfaces in packed beds of uniform spheres. Although the present work addresses only static free-surface shapes, the results are likely to yield important insights into optimal wick structures under dynamic conditions. In steady operation, liquid is fed to the evaporator section of the heat pipe from the adiabatic section with a constant mass flow rate, and constant time-independent free-surface shape results. The free-surface shape determines the capillary pressure generated, as well as important heat transfer parameters, such as the extent of the thin-film region, the total exposed area for evaporation heat transfer, and the conduction resistance of the liquid. These performance parameters are computed as functions of the microstructure geometry, the solid-liquid contact angle, and the liquid volume. A comparative study of four different well-defined microstructured surfaces is performed. The microstructure with the best performance for the evaporator section is determined from these computations. An effective thermal resistance model for the evaporator section is used to study the variation in the wick thermal resistance with changing liquid level in the pores. Based on this model, the optimum liquid level in the wick pore, which provides the greatest wicking action, as well as low thermal resistance, is identified.

2 Microstructure Topologies

Some of the common microstructured wicks used in cooling devices are made of wire meshes, sintered powders, grooves, and felts/fibers. These microstructures are generally multilayered. In this paper, the free-surface shape of the liquid filling these microstructures is assumed to be little-affected by the number of layers, and only one layer of the microstructure is considered for the four geometries studied. The porosity, defined as the ratio of void volume to the total volume, is taken to be same in all four cases. The unit cells for the four surfaces are shown in Fig. 1 and are described below.
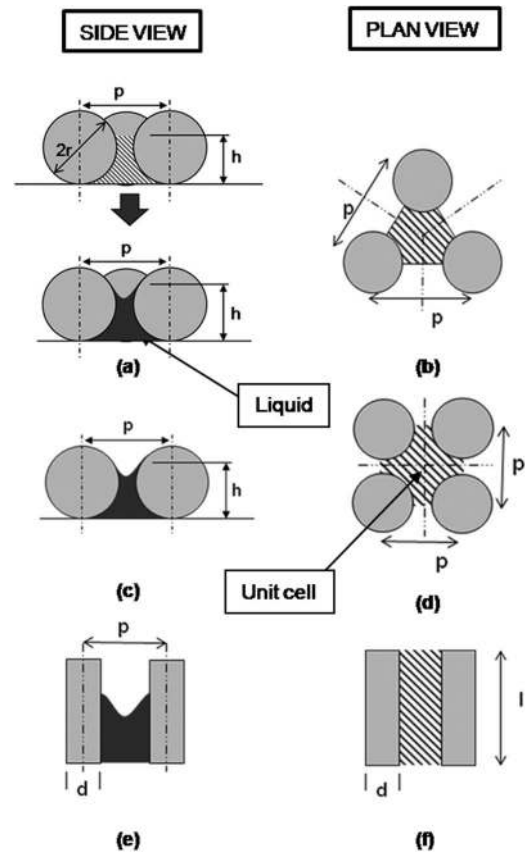
Topology 1. Uniform spheres on a surface in both hexagonal

Fig. 1 Side views of surface with (*a*) spheres (hexagonally packed), (*c*) spheres (square packed) and horizontal cylinders, (*e*) vertical cylinders, and parallel rectangular ribs. Plan views of surface with (*b*) spheres and cylinders (both hexagonally packed), (*d*) spheres and cylinders (both square packed), and (*f*) horizontal cylinders and rectangular ribs. The corresponding unit cell is also shown in each case.

packing (HP) (Figs. 1(*a*) and 1(*b*)) and square packing (SP) arrangements (Figs. 1(*c*) and 1(*d*)).

Topology 2. Surface with vertical cylinders in both hexagonal (Fig. 1(*b*)) and square packing arrangements (Figs. 1(*e*) and 1(*d*)).

Topology 3. Surface with parallel horizontal cylinders (Figs. 1(*c*) and 1(*f*)).

Topology 4. Surface with parallel horizontal rectangular ribs (Figs. 1(*e*) and 1(*f*)).

In Fig. 1(*a*), *h* is the initial height of the filling liquid measured from the substrate, and *r* is the radius of the cylinder or sphere. In Fig. 1(*f*), the length, *l*, of the cylinders and ribs is not significant, as the meniscus shape is independent of *l*. We choose *l* such that the base area of the unit cell in these cases matches the base area in Topology 1 (*SP*). The pitch, *p*, is defined as the distance between centers of adjacent spheres/cylinders/ribs. In the square-packed spheres case, we assume that the pitch is the same in both the longitudinal and transverse directions and that $p=2.4r$. This leads to a porosity of 0.64. The same porosity is maintained for all other topologies. Geometrical parameters for all topologies are shown in Table 1.

3 Problem Formulation

3.1 Wicking. The capillary pressure developed in a wick is governed by the Young–Laplace equation

Topology	L	$P(p/L)$	(base area)/L^2
1. Spheres a. HP	r	2.56	2.83
b. SP		2.4	5.75
2. Vertical cylinders a. HP	r	3.16	4.32
b. SP		2.94	8.64
3.Horizontal cylinders	r	4.32	5.75
4. Rectangular ribs	d	2.75	5.75

Fig. 2 Schematic illustration and definition of the thin-film region of a liquid meniscus formed over a sphere

$$\Delta p = \gamma_{LV}\left(\frac{1}{r_1} + \frac{1}{r_2}\right) = 2H' \gamma_{LV} \tag{1}$$

where Δp is the capillary pressure defined as $(p_{\text{liq}} - p_{\text{vap}})$, γ_{LV} is the surface tension between liquid and vapor phases, r_1 and r_2 are any two orthogonal radii of curvature at a point on the meniscus, and H' is the mean curvature at any point.

For a static liquid free surface in equilibrium with the vapor phase, in the absence of external forces (e.g., gravity), the mean curvature at any point of the free surface is constant. The mean curvature is defined by the liquid free-surface shape, which depends on the solid-liquid contact angle, the geometry of the microstructure, and the volume of liquid filling the microstructure. The capillary pressure Δp is nondimensionalized as $\Delta P = \Delta pL/ \gamma_{LV}$. Other dimensionless parameters are

$$V = \frac{v}{L^3}, \quad \text{Bo} = \frac{\rho gL^2}{\gamma_{LV}}, \quad Z = \frac{z}{L}, \quad P = \frac{p}{L}, \quad H = \frac{h}{L} \tag{2}$$

in which V is the nondimensional volume of the liquid filling the unit cell of the microstructure, as shown in Fig. 1. The Bond number, Bo, is the ratio of gravitational to surface tension forces, while the nondimensional height at any point on the meniscus in its equilibrium position is denoted by Z, and H is the nondimensional height of the liquid meniscus measured from the substrate when the meniscus is horizontal (i.e., in the nonequilibrium initial condition). The characteristic length L is taken to be the radius r of the spheres/cylinders for Topologies 1, 2, and 3, and as the width of the ribs d for Topology 4. The contact angle, θ, along with the parameters described in Eq. (2), determines the shape of the equilibrium liquid meniscus. Furthermore, the nondimensional capillary pressure ΔP is given by

$$\Delta P = 2H' L = L\frac{\Delta p}{\gamma_{LV}} + \text{Bo } Z \tag{3}$$

Thus, ΔP can be computed at any point of the meniscus for a given θ and V if Bo and Z are known.

3.2 Heat Transfer Characteristics. The most important parameters, which affect evaporation heat transfer in a wicking microstructure, are the conduction resistance offered by the filling liquid, the total exposed free-surface area for evaporation, and the extent of the liquid meniscus that is in the thin-film region. These parameters are computed from the free-surface shape of the liquid meniscus, as described in Secs. 3.2.1–3.2.3.

3.2.1 Conduction Resistance of Liquid. Heat is transferred from the solid walls (the substrate wall, as well as the microstructure surface) to the surroundings through the shortest path from the walls to the liquid free surface. This distance is indicative of the conduction resistance of the liquid. We compute the area-averaged minimum distance of the liquid free-surface from the solid walls. For each point on the meniscus, the shortest distance from the solid walls is computed and averaged over the liquid free-surface area. This quantity signifies the conduction resistance
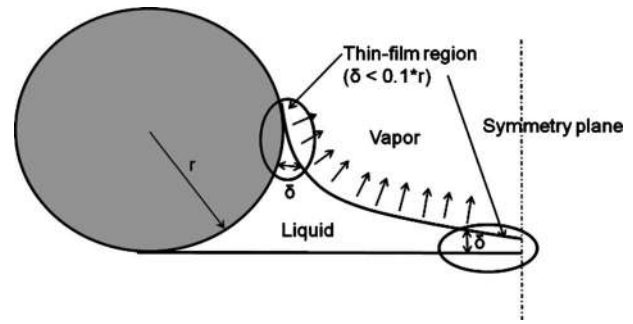
of the liquid and is computed as a function of V and θ. It is nondimensionalized by the characteristic length L of the microstructure.

3.2.2 Total Exposed Free-Surface Area. The total free-surface area of the liquid meniscus is the exposed area through which evaporation occurs and hence it is a crucial parameter for heat transfer. We compute the total free-surface area of the liquid meniscus as a function of V and θ and nondimensionalize it by the base area of the unit cell of a microstructure.

3.2.3 Thin-Film Percentage Area. The thin-film region of a liquid meniscus has been defined variously in different studies in the literature, with the width of the film ranging from 30 nm to 20 μm [24,9,15]. In the present work, we define the thin-film region based on a nondimensional thickness of $\delta=0.1*L$ (see Fig. 2). We note that the exact definition of the thin-film region is in itself not significant, since the aim of the present work is to conduct a comparative study of different microstructures. However, a range of nondimensional thin-film thickness values (defined as $0.05*L$, $0.1*L$, and $0.15*L$) are also considered in order to demonstrate the effect of this definition on the conclusions drawn here. The most common wick microstructures used in cooling devices have a characteristic length of the order of 100 μm [1]. According to our definition, therefore, the thickness of the thin-film region is on the order of 10 μm; such a region has been identified as a microregion in other studies [9]. A schematic representation of an evaporating meniscus is shown in Fig. 2. We compute the thin-film percentage area, which is defined as the percentage of the total exposed area that satisfies our thin-film definition.

The porosity is fixed at 0.64 for all the microstructures considered here. A unit cell, which defines the microstructure, is used in SURFACE EVOLVER and is explained in Sec. 4. Unit cells for different geometries are shown in Fig. 1. Only wetting liquids are considered, with wetting angles ranging from 15 deg to 90 deg. Nonwetting liquids produce unfavorable capillary pressure for evaporation and do not give rise to thin-film regions, which makes them unsuitable for evaporative heat transfer applications. The bottom wall is assumed to be perfectly wetting in all cases. Also, gravity is taken to be zero in all computations. For microstructure length scales of the order 100 μm [1], a Bond number (Bo) of the order of 10^{-3} results for a copper-water combination. This indicates that capillary forces are far greater than gravitational forces in these geometries, and that the Bond number may be assumed to be zero at such scales.

4 Numerical Approach

In the present work, we model the liquid meniscus using the program SURFACE EVOLVER [21]. SURFACE EVOLVER works on the principle of surface-energy minimization. It calculates surface energy and volume as functions of the liquid meniscus and solid configurations and evolves the free surface toward the minimum energy configuration by a gradient-descent method. SURFACE
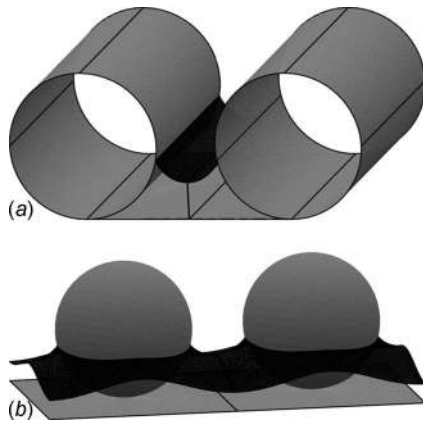
Fig. 3 Final liquid meniscus shape (dark gray) in (*a*) Topology 3, *r*=1, *V*=3.54(*H*=0.6), *P*=2.8, and θ=30 deg, and (*b*) Topology 1 (SP), *r*=1, *V*=3.6 (*H*=0.5), *P*=2.8, and θ=45 deg

Fig. 4 (*a*) $|\Delta P|_{max}$ and (*b*) maximum percentage thin-film area achieved in different topologies at any liquid volume for porosity=0.64 and θ=15 deg

EVOLVER is a powerful and computationally efficient tool for investigating liquid free surfaces in static equilibrium in complicated capillary structures. However, it should be noted that SURFACE EVOLVER cannot be used to simulate dynamic problems, that is, problems in which fluid flow occurs.

In the program, a surface is implemented as a simplical complex, i.e., a union of triangles. The energy can be due to surface tension and/or gravity or in the form of any other user-defined surface integral. SURFACE EVOLVER admits arbitrary topologies and geometrical constraints on vertex positions, as well as constraints on integral quantities, such as volume. We use the volume and level-set constraints in our modeling. The unit cell of the microstructure geometry, along with a prescribed liquid volume, is specified as the initial geometry for SURFACE EVOLVER. The free-surface shape is iterated upon, tuning the surface mesh using procedures, such as equi-angulation, vertex averaging, and mesh refinement, to obtain the final equilibrium free surface. During every iteration, SURFACE EVOLVER adjusts the vertex positions to minimize the faceted meniscus area. An equilibrium free surface is considered obtained when the surface area of the meniscus changes by less than 0.01% over 10 iterations. Figures 3(*a*) and 3(*b*) show the final surface shapes for parallel horizontal cylinders and square-packed spheres, respectively.

5 Results and Discussion

The liquid meniscus shapes for four microstructured surface topologies have been modeled using SURFACE EVOLVER. In the calculations, *V* is varied for the unit cell such that *H* varies from 0.2 to 1.8 for Topologies 1 and 3. For Topologies 2 and 4, capillary pressure and heat transfer parameters are not a strong function of *V* (except for very low values of *V*), so *V* is varied until volume independence of output parameters is achieved. The contact angle θ is varied from 15 deg to 90 deg. Efficient wicking surfaces with the highest thin-film percentage area are determined for a fixed porosity (0.64). We then present the behavior of these performance parameters with varying *V* and θ in the most efficient microstructures. Porosity is also varied for the most efficient geometry in order to understand its effect on wicking and heat transfer characteristics. A special case of low liquid volumes, which leads to a dryout condition on a part of the flat surface, is discussed. The effect of the number of layers and liquid level on wicking and heat transfer characteristics are analyzed and discussed for the case of hexagonally-packed spheres.

5.1 Free-Surface Shapes. In general, the liquid meniscus shape in any microstructure is a function of liquid volume, solid-liquid contact angle, and the surface tension between the liquid and vapor phases; the specific shape is achieved by minimizing
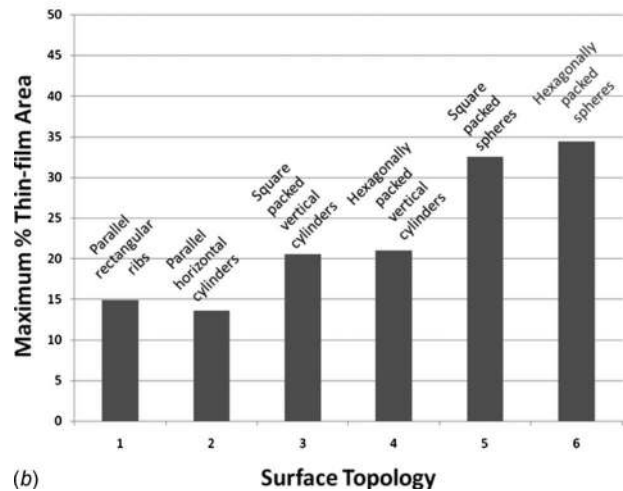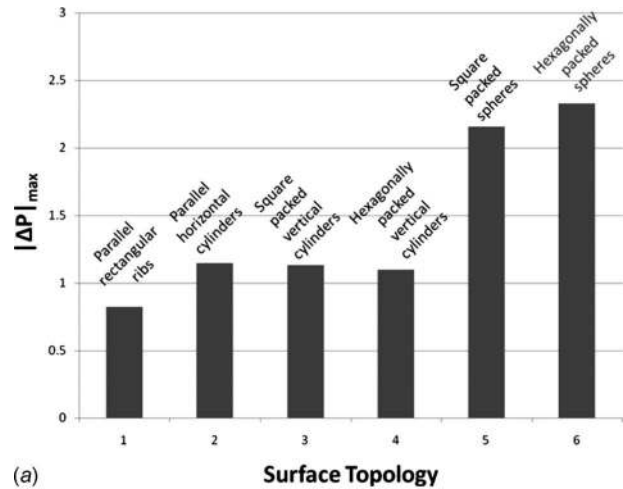
the surface-energy subject to these constraints.

In Fig. 3, we show the final liquid meniscus shapes in two topologies (3 and 1). The meniscus shape is a strong function of liquid volume in these cases. In contrast, *V* does not affect the meniscus shape in Topologies 2 and 4 except when *V* is very low (corresponding to *H*<0.2), and a dryout condition occurs on the substrate wall due to wicking action. Pore shapes in Topologies 3 and 4 are uniform in the plane parallel to substrate. Analytical expressions exist for the meniscus shapes in these topologies [22], and the meniscus is cylindrical in these cases. Pore shapes in Topologies 1 and 3 are more complex. In the case of close-packed (planar) spheres, the pore between spheres has a complex nonaxisymmetric convergent-divergent geometry, while the pore shape is nonaxisymmetric in the case of vertical cylinders. This leads to the formation of menisci that deviate significantly from spherical/cylindrical shapes. In these cases, the meniscus is puckered, exhibiting anticlastic curvature in the narrower spaces between two adjacent spheres/cylinders, while the surface is synclastic (i.e., orthogonal radii have the same sign at a point) in the central pore region. Analytical expressions for the meniscus shapes are not available in these cases and a numerical approach must be used.

5.2 Maximum Capillary Pressure and Maximum Thin-Film Percentage Area. The maximum capillary pressure ($|\Delta P|$) in all topologies is observed to be lowest for the lowest value of θ(=15 deg). Figure 4(*a*) shows the maximum $|\Delta P|$ attained in all

topologies for any liquid volume. Though ΔP is a function of liquid volume V for Topologies 1 and 3, our concern is to achieve the maximum $|\Delta P|$ irrespective of the liquid volume. From the histogram, it can be seen that the highest $|\Delta P|$ is achieved in the case of hexagonally-packed spheres on a surface. The trigonal pores formed in the case of hexagonally-packed spheres provide the smallest pore size among all microstructures for the same porosity and, hence, generate the highest capillary pressure. A similar, though somewhat lower, $|\Delta P|$ is achieved with the square-packed spheres. The highest $|\Delta P|$ achieved is nearly half of the maximum value for the rest of the microstructures considered. Thus, a surface with close-packed (planar) spheres appears to be the best wicking microstructure among all the ones considered here. Similar to the capillary pressure, the percentage thin-film area in any topology is found to be maximum for the smallest contact angle ($\theta = 15$ deg). Again, the histogram in Fig. 4(b) shows the maximum attainable percentage thin-film area in different topologies irrespective of the liquid volume. The maximum thin-film area is again achieved by close-packed (planar) spheres (Topology 1). Use of a lower value of the nondimensional thin-film thickness ($\delta = 0.05 * L$) to define the thin-film region was found to result in a decreased thin-film percentage area for all microstructures; conversely, use of a higher value of $0.15 * L$ for thin-film thickness resulted in an increased thin-film percentage area as expected. However, the definition adopted for nondimensional thin-film thickness is not found to affect the conclusions drawn from this comparative study of microstructures. The maximum thin-film percentage area is always observed to occur for hexagonally close-packed spheres on a surface. The maximum thin-film percentage area for the three cases is 19.02% ($0.05 * L$), 34.39% ($0.1 * L$), and 48.01% ($0.15 * L$).

5.3 Performance Parameters for Packed Spheres on a Surface (HP and SP Configurations). As shown in Fig. 4, packed spheres on a surface are the best class of microstructures from wicking and thin-film evaporation points of view. We find that the values of conduction resistance of the filling liquid and the total exposed surface area are less sensitive to the choice of microstructure. Therefore, the best performing microstructure is decided on the basis of the maximum capillary pressure and maximum thin-film area condition. We now present in detail the behavior of wicking and heat transfer parameters with respect to θ and V for the packed-sphere topology for a porosity of 0.64. This will lead to a determination of V for the best wicking and heat transfer performance.

5.3.1 Capillary Pressure. Figure 5 shows the variation in ΔP with V for square- and hexagonally-packed spheres. Each curve represents a different contact angle θ. A negative value of ΔP implies suction, and is desirable for wicking. For each curve and for each type of packing, we observe that the nondimensional capillary pressure reaches its minimum value at a certain liquid volume. ΔP first decreases with increasing liquid volume (or increasing H) and reaches a minimum near V corresponding to $H = 1$. For a contact angle of 15 deg, ΔP decreases from point (a) to (b) (see Fig. 5), as the liquid meniscus develops increasing net positive curvature. ΔP is minimum at point (b), which lies between a liquid height H of 0.8 and 1. As V increases from 0 to 1.5, the pore size between spheres continues to decrease and hence the absolute capillary pressure increases. In the larger pore spaces between spheres, the meniscus develops synclastic curvature (i.e., the curvatures in orthogonal directions at a point have the same sign) while being saddle-shaped or anticlastic in the narrower spaces between spheres. The net curvature reaches a maximum at point (b). With increasing volume ($H > 1, V > 1.5$), ΔP starts to increase as the pore size continues to increase and hence the meniscus curvature decreases. ΔP reaches its maximum at point (c) where the meniscus curvature is lowest. It is interesting to note that positive capillary pressure can be achieved with high wetting
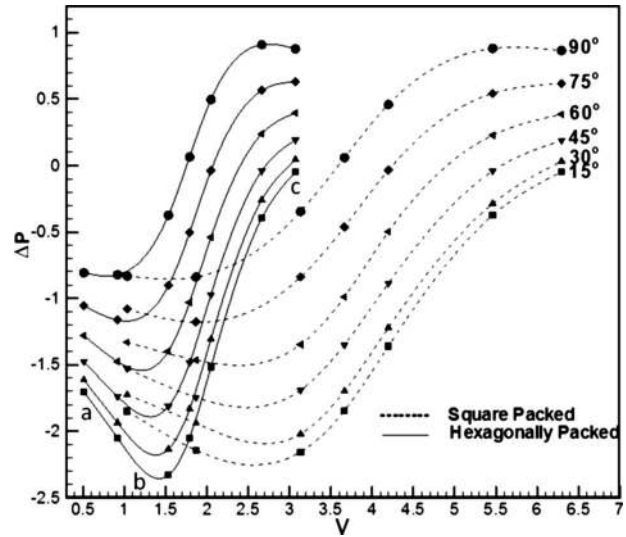

Fig. 5 Capillary pressure versus nondimensional liquid volume for square and hexagonally-packed spheres for various contact angles (15–90 deg)

contact angles (>30 deg) when V is high (corresponding to $H > 1.2$, in general). A maximum $|\Delta P|$ is attained in the hexagonally-packed case for $\theta = 15$ deg near $V = 1.5$ (corresponding to $H \sim 1$), and this is the desired operating condition for maximum wicking. Dryout on the flat surface is observed for the lowest contact angle (15 deg) in the square packing arrangement. Dryout conditions due to wicking will be discussed further in Sec. 5.5.

5.3.2 Thin-Film Percentage Area. The percentage of the total exposed area defined as a thin film is presented in Figs. 6(a) and 6(b) as a function of V and θ in the HP and SP arrangements, respectively. A higher thin-film area is obtained for smaller contact angles. Also, the percentage thin-film area is the highest for the smallest liquid volumes. This is because for low liquid volumes, the liquid meniscus shape is similar to the one shown in Fig. 2, and the thin-film condition is satisfied both at the sphere and the unit-cell substrate surface. However, in the hexagonally-packed case, the thin-film condition is not satisfied at the substrate surface for higher contact angles (>60 deg) and lower values of $V (<1)$. As we increase V, the bottom wall stops contributing to the thin-film area and the percentage thin-film area decreases. However, it again reaches a maximum at a certain V. It is clear that if the substrate wall is not taken into consideration for the meniscus distance computations, we would obtain a perfectly symmetric curve with a maximum in the middle. Again, we observe that the maximum percentage thin-film area is achieved in the hexagonally-packed case near $V = 1.5$. Hence, we conclude that $V = 1.5$ and $\theta = 15$ deg in the hexagonally-packed case provides the maximum wicking, as well as the maximum thin-film area.

5.3.3 Area-Averaged Minimum Meniscus Distance. As discussed before, the area-averaged minimum meniscus distance from the solid surface is a measure of the heat conduction resistance of the liquid filling the microstructure. Figure 7 shows the variation in this quantity with V for square- and hexagonally-packed spheres on a surface. Each curve represents a different contact angle θ. It can be observed from the curves that the distance is smaller for lower contact angles and lower liquid volumes. This is again because of the substrate-wall effect for lower liquid volumes. The wall effect can be observed for $H < 0.5$ in both packing arrangements. The resistance increases as we further increase V and reaches a maximum. Once the substrate wall no

Fig. 7 Non-dimensional area-averaged minimum meniscus distance versus nondimensional liquid volume for square- and hexagonally-packed spheres for various contact angles (15–90 deg)
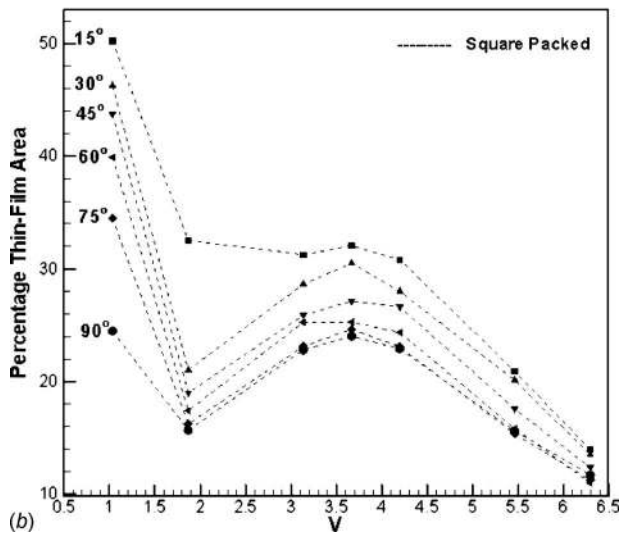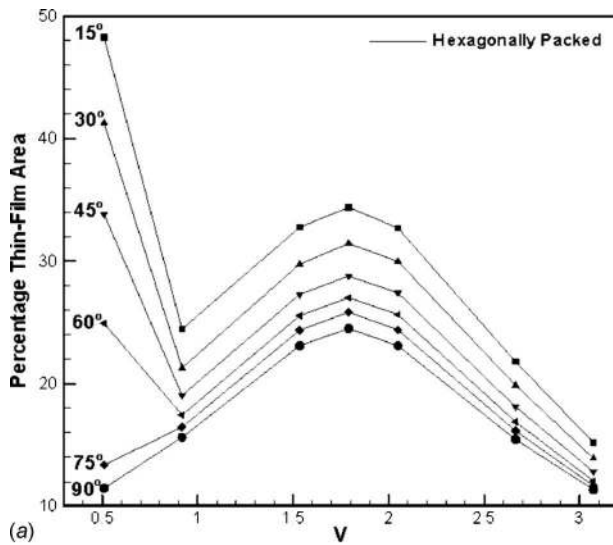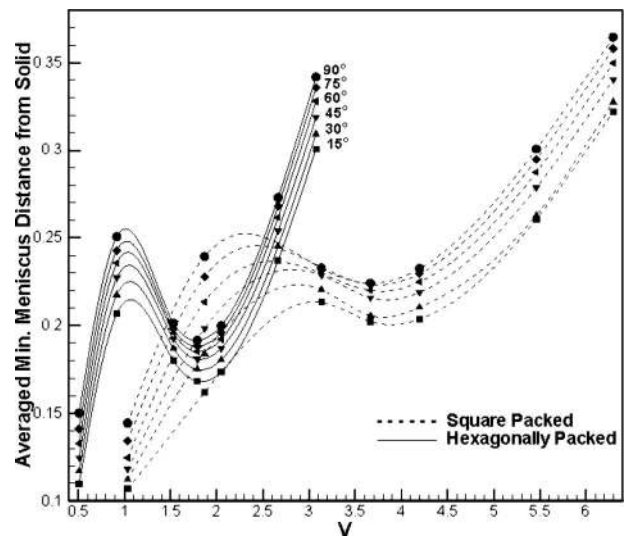
Fig. 6 Percentage thin-film area versus nondimensional liquid volume for (a) hexagonally packed and (b) square-packed spheres for various contact angles (15–90 deg)

serve that the exposed area for evaporation is lowest near $V=1.5$. Hence, a trade-off exists, and the optimum value of V can be obtained by minimizing a formal cost function formulated by assigning appropriate weights to the various performance parameters.

5.4 Effect of Porosity. We now address wicking and heat transfer characteristics for hexagonally-packed spheres as a function of microstructure porosity. Iverson et al. [1] used wick samples with porosities ranging from 0.46 to 0.6. We vary porosity from 0.39 (corresponding to the case of close hexagonally-packed spheres) to 0.64, with $\theta=15$ deg held constant for all cases. Figures 9(a) and 9(b) show, respectively, the maximum $|\Delta P|$ and the maximum percentage thin-film area achieved at any porosity, irrespective of the liquid volume. It is observed that, as would be expected, a lower porosity leads to a higher capillary

longer has the shortest path to the liquid free surface, the resistance value is characterized only by the distance between the meniscus and the sphere surface. This distance starts decreasing with increase in V and attains a second minimum at a liquid volume corresponding to $H\sim1$. It can be observed that the hexagonally-packed case gives a very low conduction resistance near $V=1.5$, which was also found to be the volume for which the highest capillary pressure and high thin-film area were obtained.

5.3.4 Exposed Surface Area. The total liquid free-surface area exposed to evaporation, nondimensionalized by the base area of the unit cell, is presented in Fig. 8 as a function of V and θ in the SP and HP arrangements. The total free-surface area increases with decreasing θ and for each θ, it decreases as we increase V, with a minimum achieved at $H\sim1$. This is because initially the effective pore radius decreases as we increase H from 0 to 1. However, the pore radius increases as we increase H from 1 to 2. It can be observed that the minimum occurs near $V=1.5$ for the hexagonally-packed case. From the variation in capillary pressure, percentage thin-film area, and conduction resistance of the filling liquid (Figs. 5–7) for hexagonally-packed spheres on a surface, the optimum operation point for maximum evaporation appears to occur at $\theta=15$ deg near $V=1.5$. However, from Fig. 8, we ob-
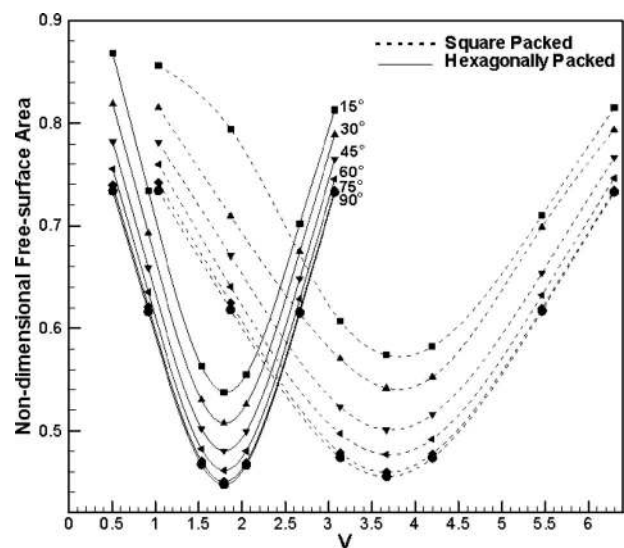

Fig. 8 Total exposed liquid free-surface area versus nondimensional liquid volume for square- and hexagonally-packed spheres for various contact angles (15–90 deg)
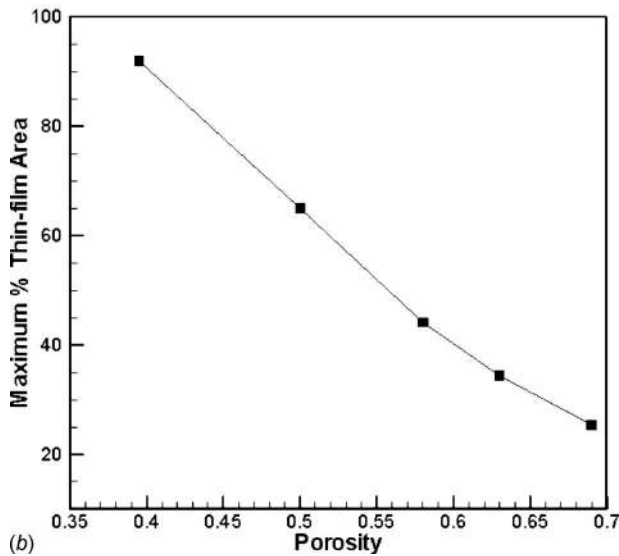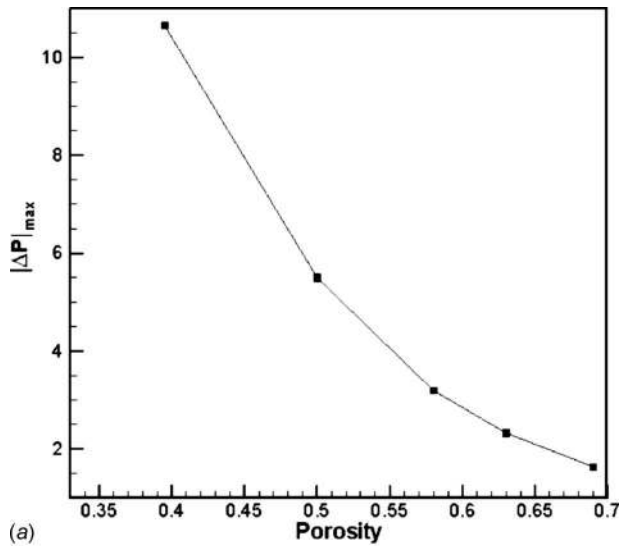
Fig. 10 Final liquid meniscus shape (dark gray) for (a) Topology 3, r=1, V=1.58(H=0.2), P=2.8; θ=15 deg between cylinder surface and liquid and θ=15 deg between bottom surface and liquid, and (b) Topology 1 (SP), r=1, V=0.75(H=0.1), P=2.8; θ =15 deg between sphere's surface and liquid, and θ=0 deg between the bottom surface and liquid

Fig. 9 (a) Maximum |ΔP| and (b) maximum percentage thin-film area versus porosity in hexagonally-packed spheres on a surface, θ=15 deg

pressure and a higher thin-film percentage area. Hence, the closest packed case is the ideal case for wicking and also provides the largest thin-film area.

5.5 Special Case of Low Liquid Volumes. When the volume of the liquid filling the microstructure is very low (corresponding to $H < 0.2$) and the contact angle is small (≤ 15 deg), a part of the bottom wall may dry out due to wicking. We show two such cases in Figs. 10(a) and 10(b). It is observed that the liquid is wicked up on to the cylinder/sphere surface, and a part of the bottom wall is depleted of liquid, depending on the contact angle between the liquid and bottom wall surface. Figure 10(a) shows a case with a contact angle of $\theta=15$ deg between the solid surfaces and the liquid. Under this condition, the liquid free surface breaks up at the symmetry plane between adjacent cylinders and moves toward the cylinder surface. Figure 10(b) shows the case of square-packed spheres when the bottom surface is perfectly wetting. In this case, a part of the bottom surface is perfectly wetted and the liquid recedes from the sphere surface. Since a perfectly wetting surface is difficult to achieve, dryout situations are expected to be more common with low liquid volumes. It should be noted that very low liquid volumes are unfavorable for heat transfer applica-
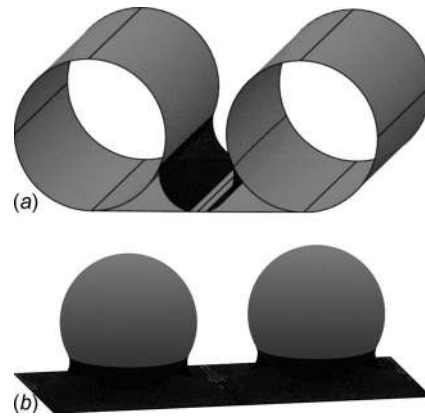
tions, as the portions that dry out do not contribute to evaporation heat transfer, and heat loss in these regions would be due to natural convection alone.

5.6 Effect of Number of Layers. The number of sphere layers typically used in sintered-copper wicks is approximately 8–10. The effect of the number of layers on the static meniscus shapes and heat transfer parameters must be understood in order to simulate heat pipe conditions. Two layers of spheres in the microstructure (Topology 1, HP) are considered now. Liquid meniscus shapes in the second layer of spheres are computed and the four performance parameters (capillary pressure, thin-film percentage area, area-averaged minimum meniscus distance and total meniscus area) are obtained as functions of H (initial liquid level in the second layer). A hexagonal packing arrangement is assumed for every layer of spheres since it provides the maximum wicking and thin-film percentage area. In the vertical direction, a simple-cubic packing arrangement is assumed. The final meniscus shape for one such case is shown in Fig. 11.

A porosity of 0.56, corresponding to $P=1.28$, is chosen, corresponding to the average porosity (range of porosity=0.46–0.6 [1]) of practical wicks (Topology 1, HP). It is observed that the liquid meniscus shapes formed in the second layer of spheres remain unaffected by the lower layer of spheres and are only determined by the second layer's configuration. This is why the capillary pressure and exposed meniscus area do not change for the second layer from those for single layers. However, the area-averaged minimum meniscus distance and thin-film percentage area are different for the second layer of spheres when $H < 0.5$
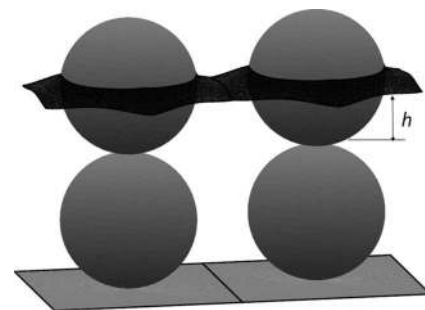

Fig. 11 Final liquid meniscus shape (dark gray) for Topology 1 (HP), r=1, H=1, P=2.8; θ=15 deg between sphere surface and liquid
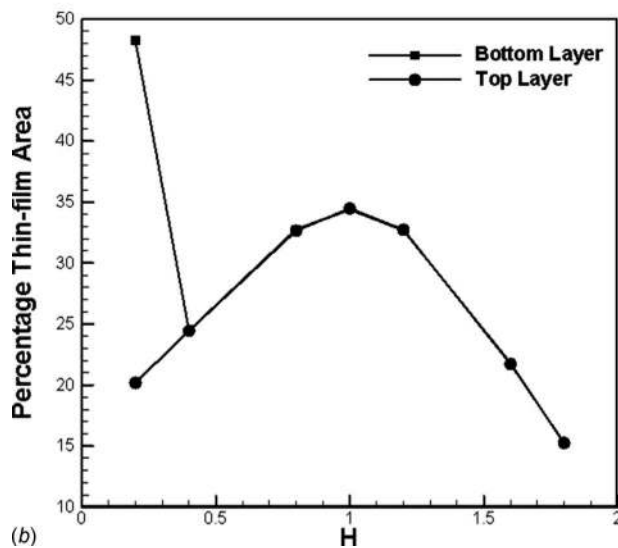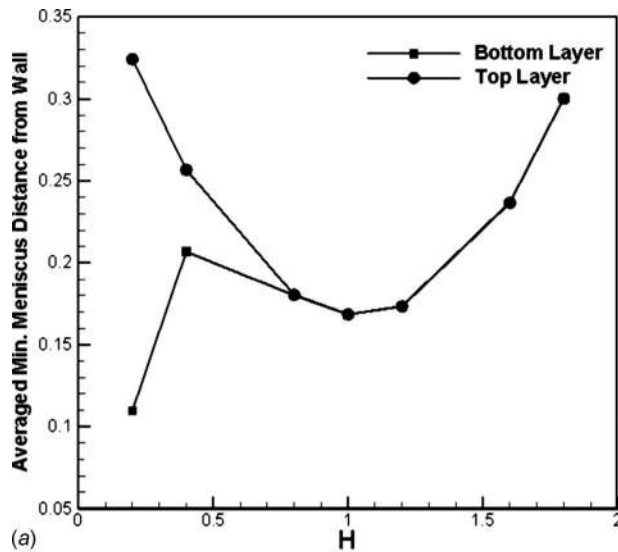
Fig. 12 (*a*) Area-averaged meniscus distance from solid walls versus nondimensional liquid height, and (*b*) percentage thin-film area of the meniscus for top and bottom layers of spheres in two-layer configuration versus nondimensional liquid height; $\theta = 15$ deg, porosity = 0.56

Fig. 13 (*a*) Thermal resistance model for heat transfer in a wick (shown for hexagonally-packed spheres on a surface with simple-cubic packing in the *z*-direction), and (*b*) equivalent resistance network

(Figs. 12(*a*) and 12(*b*)). This is because of the presence of spheres below the liquid meniscus formed in the second layer of spheres. This affects the minimum meniscus distance from the solid walls.

5.7 Effective Thermal Resistance of the Wick. As discussed earlier, liquid meniscus shape is a strong function of the liquid level (*H*) in hexagonally-packed spheres (Topology 1, HP). We observed that $V = 1.5$ corresponds to maximum capillary pressure for a single layer of spheres and also yields a small conduction resistance and a high thin-film percentage area. Nevertheless, the exposed meniscus area is nearly the smallest at this value of *V*. Hence, determination of the optimum liquid level for any layer of spheres requires the formulation of a cost function for wick performance as a function of *H*. The optimum liquid volume can also be determined if optimum *H* and *N* are known. The two important parameters for the performance of wick microstructures in cooling devices are their maximum wicking capability and the thermal resistance: The optimum liquid level is that which provides maximum wicking, as well as the lowest thermal resistance for conduction and evaporation heat transfer.
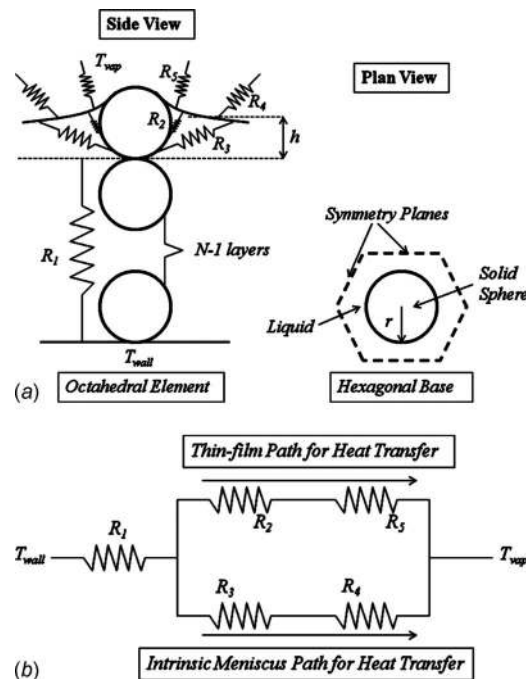
In Fig. 13(*a*), an approximate thermal resistance model for conduction and evaporation through the wick in Topology 1 (HP) is shown. An octahedral volume around a sphere is chosen as the representative unit cell. A three-dimensional packing of spheres, similar to the one discussed in the two-layer configuration, is assumed. Heat flows from the hot bottom wall to the liquid-vapor interface by conduction. For the present analysis, convection can be ignored in comparison to conduction through the solid sintered material. Also, thermocapillary convection is not considered. Heat transfer from liquid to vapor occurs at the interface by evaporation. The five thermal resistances R_1, R_2, R_3, R_4, and R_5, as shown in Fig. 13(*a*), result from (i) the conduction resistance due to ($N - 1$) layers of spheres (solid) and interstitial liquid, (ii) the thermal resistance offered by the liquid for conduction from the top layer of spheres to meniscus, and (iii) the evaporation resistance of the liquid meniscus. Temperature varies along the liquid meniscus because of the variation in evaporation rate resulting from the variations in film thickness. In the present model, the liquid meniscus is assumed to be at two different temperatures, one corresponding to the thin-film region, and the other to rest of the meniscus. Hence, there are two separate paths, viz., the thin-film path and the intrinsic meniscus path (or the non-thin-film path), for heat transfer from the top layer of spheres to the vapor. These resistances can be represented in terms of the three heat transfer parameters computed from the static meniscus shape. We have used a functional notation for the three heat transfer parameters, viz., $F_1(h)$ for nondimensional area-averaged minimum meniscus distance, $F_2(h)$ for nondimensional meniscus area, and $F_3(h)$ for percentage thin-film area. The resistance R_1 is the thermal resistance due to ($N-1$) layers of spheres and interstitial liquid; R_2 is the thermal resistance offered by the liquid between the sphere wall and the thin-film region; R_3 is the thermal resistance offered by the liquid between the sphere wall and the intrinsic region of the meniscus (i.e., the non-thin-film region); R_4 is the thermal resistance accounting for evaporation from the intrinsic meniscus

region; and R_5 is the thermal resistance accounting for evaporation from the thin-film region of the meniscus. The definitions of these resistances are given below

$$R_1 = \frac{(N-1)2r}{k_{\text{eff}}\text{area}_{\text{hexagon}}r^2}, \quad R_2 = \frac{0.1r}{2k_w(0.01F_2F_3)r^2}$$

$$R_3 = \frac{(F_1F_2 - 0.001F_2F_3)r}{(F_2 - 0.01F_2F_3)^2k_w2r^2} \quad (4)$$

$$R_4 = \frac{1}{h_{\text{meniscus}}(F_2 - 0.01F_2F_3)(2r^2)}$$

$$R_5 = \frac{1}{h_{\text{meniscus}}(0.01F_2F_3)(2r^2)}$$

The values used in the above expressions are now discussed. The number of sphere layers is taken to be $N=10$, the radius of spheres is assumed to be $r=100$ μm, and the porosity is assumed to be 0.56. area$_{\text{hexagon}}$ is the base area of the octahedral volume shown in Fig. 13(a). The effective thermal conductivity k_{eff} of a sphere-liquid layer is obtained using FLUENT [25] and is found to be 42.8 W/m K for a copper-water combination ($k_w=0.6$ W/m K, $k_{\text{cu}}=387.6$ W/m K). It should be noted that the analysis presented later using this resistance model is independent of R_1 and so the details of the computation of k_{eff} are not included here. h_{meniscus} is the convective heat transfer coefficient accounting for evaporation from the meniscus and is taken to be 10^6 W/m^2 K [9]. We note that the present model does not account for contact resistance between the spheres.

Figure 13(b) shows the thermal resistance network for heat transfer in the wick. The total or effective thermal resistance of the wick is calculated using

$$R_{\text{eff}} = R_1 + \frac{(R_2 + R_5)(R_3 + R_4)}{(R_2 + R_3 + R_4 + R_5)} \quad (5)$$

The effective thermal resistance (R_{eff}) of the wick for conduction and evaporation can now be represented in terms of $F_1(h)$, $F_2(h)$, and $F_3(h)$. Optimization of the liquid level, h, is performed by creating a cost function and assigning equal weights to capillary pressure and heat transfer. This cost function is minimized to achieve maximum $|\Delta P|$ and minimum thermal resistance, R_{eff}.

5.8 Optimum Liquid Level in the Wick Pore. Figure 14(a) shows the variation of resistances with nondimensional liquid level, H. Variations are shown for a solid-liquid contact angle of 45 deg. It is observed that R_1 is independent of the liquid level. Also, it is smaller than R_2 and R_3. R_2 and R_3 are quite large due to the very small meniscus area. At $H=1$, R_2 is lowest because of highest thin-film area at this H value. R_3 is highest at $H=1$ because of lowest total meniscus area at this liquid level. R_4 and R_5 (evaporative resistances) are very small compared with other resistances. R_4 (due to evaporation from intrinsic meniscus) is smaller than R_5 (due to thin-film evaporation) because the thin-film area is much smaller than the intrinsic meniscus area.

Figure 14(b) shows the variation in the thermal resistances in the thin-film and non-thin-film paths with changing H. It is observed that the thin-film path resistance is lowest at $H=1$ because the thin-film percentage area reaches a maximum at this meniscus position (Figs. 6(a) and 12(b)). However, the non-thin-film path resistance attains a maximum at $H=1$ because the exposed meniscus area is minimum at this H value. The latter leads to the maximum in R_{eff} seen at $H=1$. When H is in the range of 0.8–1.2, the thin-film path gives a lower resistance to heat flow than the intrinsic meniscus or non-thin-film path, indicating that more than 50% of heat transfer occurs through the thin-film portion of liquid meniscus. At other values of H, more than 30–40% of heat transfer occurs from the thin-film region. Thin-film evaporation is sup-
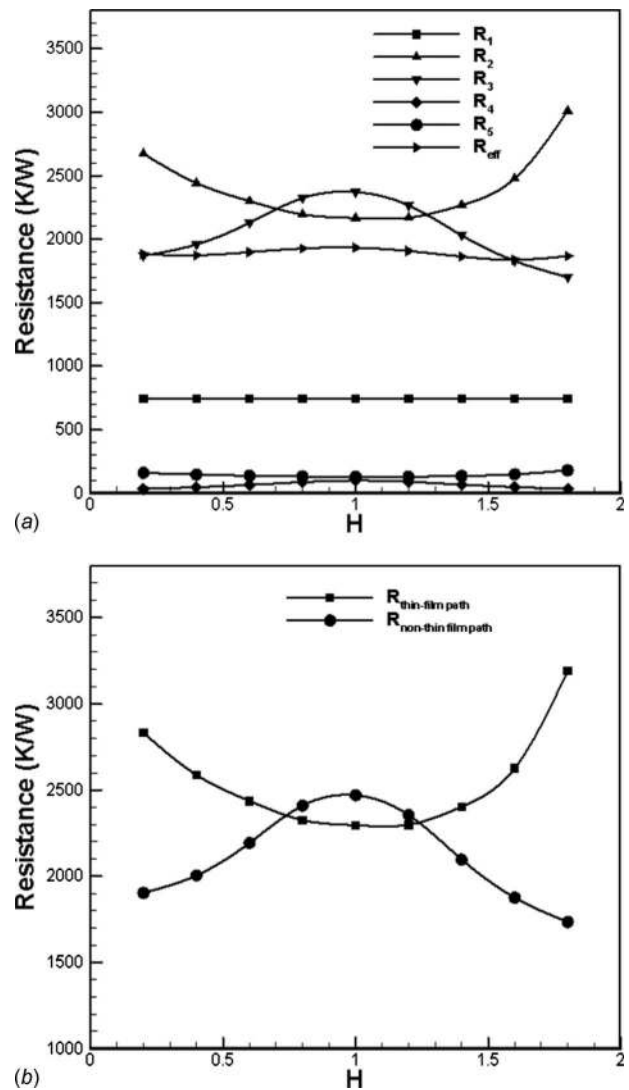

(a)

(b)

Fig. 14 (a) Thermal resistance variation with nondimensional liquid level (H) in the wick pore, and (b) thermal resistances in thin-film and non-thin-film (extrinsic meniscus) paths for heat transfer versus nondimensional liquid level; $\theta=45$ deg, porosity=0.56

pressed at H values other than those in the range of 0.8–1.2. However, the total heat transfer is governed by the total resistance, R_{eff}.

The variation of R_{eff} with H is shown in Fig. 15 for a porosity of 0.56 and for $\theta=15$, 30, and 45 deg. It is observed that effective resistance to heat transfer is lowest for the lowest contact angle. Also, the effective thermal resistance at any contact angle is highest when liquid fills the wick pore half-way through, i.e., $H=1$. Although the thin-film resistance is lowest at $H\sim1$, the total resistance is highest here because of the smallest total meniscus area. The total resistance increases beyond $H\sim1.6$ as the thin-film area decreases drastically in the range $H=1.6$–1.8. R_{eff} exhibits two minima for higher values of contact angle as H varies from 0.2 to 1.8 while only one minimum is observed in case of lower contact angles (<30 deg). R_{eff} is a combination of the resistances in the thin-film and non-thin-film paths. The variation in R_{eff} depends on how these resistances change with H. The variations in thin-film and non-thin-film path resistances with H are governed by the corresponding variations in thin-film area and total meniscus area and are presented in Fig. 14(b). As can be observed in Fig. 14(b), for a contact angle of 45 deg, the thin-film path resis-
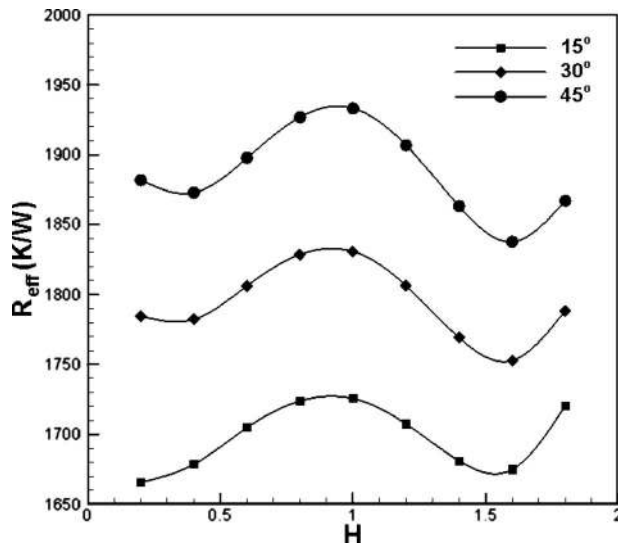
Fig. 15 Total thermal resistance for evaporation and conduction in the wick versus nondimensional liquid height in the wick pore for θ=15, 30, and 45 deg, porosity=0.56

tance decreases while the non-thin-film path resistance increases as H varies from 0.2 to 0.5. The decrease in thin-film path resistance compensates and swamps the increase in non-thin-film path resistance, and leads to an overall decrease in R_{eff}. Therefore, a minimum in the R_{eff} curve is observed near $H \sim 0.5$. This minimum is not observed in case of the 15 deg contact angle because the decrease in thin-film path resistance for 15 deg fails to overcome the increase in non-thin-film path resistance. The second minimum in R_{eff} is observed at $H \sim 1.5$ for all contact angles and is caused by the increase in thin-film path resistance as H increases from 1.5 to 1.8 (Fig. 14(b)).

An important point to note here is that the maximum percentage change in R_{eff} with the variation in H is only about 5% at any contact angle. However, $|\Delta P|$ varies from 0 (minimum) to 3.2 (maximum) with H for θ=15 deg and porosity=0.56. Hence, the variation in liquid level in the wick pore does not affect the total heat transfer from the wick as much as it affects the capillary pressure. Therefore, the optimum liquid level should be determined based on the capillary pressure variation with meniscus height and is found to be optimum at $H \sim 0.8-1$ ($V \sim 1.5$, Topology 1, HP).

6 Conclusions

The wicking and heat transfer characteristics of four well-defined microstructures have been studied by computing the static liquid free-surface shapes using SURFACE EVOLVER. The wicking characteristics of the microstructure are characterized by the capillary pressure. The heat transfer characteristics of the static liquid meniscus are characterized by the percentage of the liquid meniscus that is in the thin-film region, the conduction resistance of the liquid, and the total exposed surface area of the meniscus for evaporation. The solid-liquid contact angle and the liquid volume are varied for all microstructures to determine the most efficient geometry for evaporation. Among all the microstructures considered, hexagonally-packed uniform spheres on a surface are found to generate the maximum favorable capillary pressure for evaporation at a contact angle of θ=15 deg. The liquid meniscus is also found to possess the maximum thin-film area for this case. We have studied the effect of contact angle and liquid volume variation on wicking and heat transfer performance for packed spheres on a surface. The effects of porosity and low liquid volumes in the microstructure are also presented. The effect of the number of sphere layers in Topology 1 (HP) on wicking, and heat transfer

performance is investigated. Finally, a thermal resistance model of the wick is proposed and the optimum liquid level H in the wick pore is obtained for maximum wicking and heat transfer. The main conclusions drawn from the study of packed spheres (Topology 1) on a surface are as follows.

- Capillary pressure and heat transfer parameters are strong functions of θ and V. The highest favorable capillary pressure is realized for the hexagonally-packed case.
- For high values of $V(H>1.2)$, positive and hence unfavorable capillary pressure for evaporation can be generated even for wetting contact angles (30 deg$<\theta<$90 deg). This condition must be avoided for efficient device operation.
- V=1.5 is the optimum liquid volume for maximum wicking (θ=15 deg) for the case of hexagonally-packed spheres. The highest thin-film percentage area and the lowest liquid conduction resistance are also observed at the same value of V. However, the exposed surface area of the liquid meniscus is near its minimum for V=1.5. Hence, an optimum V must be determined to maximize overall performance.
- Capillary pressure and percentage thin-film area increase with decreasing porosity. Hence, hexagonal close-packed spheres on a surface appear to be the most favorable geometry for evaporation. However, this arrangement also offers the maximum resistance to flow. Permeability is thus an important factor in determining the optimum wick porosity. This consideration will be a part of our future investigations.
- The static liquid meniscus shape does not depend on the number of layers of spheres in the wick but only depends on the sphere arrangement at the liquid free surface. Hence, the wick pores at the free surface determine the capillary pressure and thin-film characteristics of the liquid meniscus.
- An approximate effective thermal resistance model developed for the wick (Topology 1, HP) shows that wick heat transfer performance is nearly independent of the liquid level in the wick pore. Hence, the optimum liquid level should be determined on the basis of capillary pressure variation with liquid level and is found to be $H \sim 0.8-1$ at any porosity.

Nomenclature

area$_{\text{hexagon}}$ = base area of octahedral volume used in effective resistance model
Bo = Bond number ($=\rho g L^2 / \gamma_{LV}$)
d = width of rectangular ribs
D = dimensionless width of rectangular ribs
F = notation for heat transfer parameters associated with free surface of the liquid meniscus
g = acceleration due to gravity
h = height of liquid free-surface from substrate
h_{meniscus} = convective heat transfer coefficient of meniscus accounting for evaporation
H = dimensionless height of liquid free-surface ($=h/L$)
H' = mean curvature of meniscus at any point
HP = hexagonally-packed configuration
N = number of sphere layers for hexagonally-packed spheres
k = thermal conductivity
l = length of cylinders/ribs in unit cell
L = characteristic length
p = pitch
P = dimensionless pitch ($=p/L$)
P_{liq} = liquid pressure
P_{vap} = vapor pressure
r = radius of cylinders/spheres
r_1, r_2 = orthogonal radii of curvature at any point on liquid meniscus

R = notation for thermal resistances in effective thermal resistance model

SP = square-packed configuration

v = liquid volume filling unit cell measured from substrate

V = dimensionless liquid volume ($=v/L^3$)

z = height of any point on liquid meniscus from substrate

Z = dimensionless height of any point on liquid meniscus ($=z/L$)

Greek

Δp = capillary pressure

ΔP = nondimensional capillary pressure ($=L\Delta p/\gamma_{LV}$)

γ_{LV} = surface tension between liquid and vapor phases

ρ = density of liquid

θ = contact angle between liquid and solid surfaces

Subscripts

cu = copper

eff = effective

max = maximum

w = water

References

[1] Iverson, B. D., Davis, T. W., Garimella, S. V., North, M. T., and Kang, S. S., 2007, "Heat and Mass Transport in Heat Pipe Wick Structures," J. Thermophys. Heat Transfer, **21**(2), pp. 392–404.

[2] Davis, T. W., and Garimella, S. V., 2008, "Thermal Resistance Measurement Across a Wick Structure Using a Novel Thermosyphon Test Chamber," Exp. Heat Transfer, **21**, pp. 143–154.

[3] Bauer, T. H., 1993, "General Analytical Approach Toward the Thermal Conductivity of Porous Media," Int. J. Heat Mass Transfer, **36**(17), pp. 4181–4191.

[4] Abo El-Nasr, A., and El-Haggar, S. M., 1996, "Effective Thermal Conductivity of Heat Pipes," Heat Mass Transfer, **32**(1–2), pp. 97–101.

[5] Garimella, S. V., and Sobhan, C. B., 2001, "Recent Advances in the Modeling and Applications of Nonconventional Heat Pipes," Adv. Heat Transfer, **35**, pp. 249–308.

[6] Gupta, A., and Upadhya, G., 1999, "Optimization of Heat Pipe Wick Structures for Low Wattage Electronics Cooling Applications," *Advances in Electronic Packaging 1999, Pacific RIM/ASME International Intersociety Electronics Photonic Packaging Conference*, ASME, New York, **26**, pp. 2129–2137.

[7] Abhat, A., and Seban, R. A., 1974, "Boiling and Evaporation From Heat Pipe Wicks With Water and Acetone," ASME J. Heat Transfer, **96**(3), pp. 331–337.

[8] Hanlon, M. A., and Ma, H. B., 2003, "Evaporation Heat Transfer in Sintered Porous Media," ASME J. Heat Transfer, **125**, pp. 644–652.

[9] Wang, H., Garimella, S. V., and Murthy, J. Y., 2007, "Characteristics of an Evaporating Thin Film in a Microchannel," Int. J. Heat Mass Transfer, **50**, pp. 3933–3942.

[10] Wang, H., Garimella, S. V., and Murthy, J. Y., 2008, "An Analytical Solution for the Total Heat Transfer in the Thin-film Region of an Evaporating Meniscus," Int. J. Heat Mass Transfer, **51**, pp. 6317–6322.

[11] Vadakkan, U., Garimella, S. V., and Murthy, J. Y., 2004, "Transport in Flat Heat Pipes at High Heat Fluxes From Multiple Discrete Sources," ASME J. Heat Transfer, **126**, pp. 347–354.

[12] Kim, S. J., Seo, J. K., and Do, K. H., 2003, "Analytical and Experimental Investigation on the Operational Characteristics and the Thermal Optimization of a Miniature Heat Pipe With a Grooved Wick Structure," Int. J. Heat Mass Transfer, **46**, pp. 2051–2063.

[13] Do, K. H., Kim, S. J., and Garimella, S. V., 2008, "A Mathematical Model for Analyzing the Thermal Characteristics of a Flat Micro Heat Pipe With a Grooved Wick," Int. J. Heat Mass Transfer, **51**(19–20), pp. 4637–4650.

[14] Mwaba, M. G., Huang, X., and Gu, J., 2006, "Influence of Wick Characteristics on Heat Pipe Performance," Int. J. Energy Res., **30**, pp. 489–499.

[15] Xu, X., and Carey, V. P., 1990, "Film Evaporation From a Micro-Grooved Surface—An Approximate Heat Transfer Model and Its Comparison With Experimental Data," J. Thermophys. Heat Transfer, **4**, pp. 512–520.

[16] Ma, H. B., and Peterson, G. P., 1997, "Temperature Variation and Heat Transfer in Triangular Grooves With an Evaporating Film," J. Thermophys. Heat Transfer, **11**, pp. 90–97.

[17] Morris, S. J. S., 2001, "Contact Angles for Evaporating Liquids Predicted and Compared With Existing Experiments," J. Fluid Mech., **432**, pp. 1–30.

[18] Morris, S. J. S., 2003, "The Evaporating Meniscus in a Channel," J. Fluid Mech., **494**, pp. 297–317.

[19] Wang, H., Murthy, J. Y., and Garimella, S. V., 2008, "Transport From a Volatile Meniscus Inside an Open Microtube," Int. J. Heat Mass Transfer, **51**, pp. 3007–3017.

[20] Dhavaleswarapu, H. K., Chamarthy, P., Garimella, S. V., and Murthy, J. Y., 2007, "Experimental Investigation of Steady Buoyant-Thermocapillary Convection Near an Evaporating Meniscus," Phys. Fluids, **19**, p. 082103.

[21] Brakke, K. A., 1992, "The Surface Evolver," Exp. Math., **1**(2), pp. 141–165.

[22] Hilden, J. L., and Trumble, K. P., 2003, "Numerical Analysis of Capillarity in Packed Spheres: Planar Hexagonal-Packed Spheres," J. Colloid Interface Sci., **267**, pp. 463–474.

[23] Slobozhanin, L. A., Alexander, J. I. D., Collicott, S. H., and Gonzalez, S. R., 2006, "Capillary Pressure of a Liquid in a Layer of Square-Packed Uniform Spheres," Phys. Fluids, **18**(8), p. 082104.

[24] Potash, M., Jr., and Wayner, P. C., 1972, "Evaporation From a 2-Dimensional Extended Meniscus," Int. J. Heat Mass Transfer, **15**(10), pp. 1851–1863.

[25] Fluent Inc., 2004, FLUENT 6.2 User's Guide.